Transition Analysis for the HIFiRE-5 Vehicle

Meelan Choudhari[*], Chau-Lyan Chang[*], Thomas Jentink[**], Fei Li[*], Karen Berger[***]
NASA Langley Research Center, Hampton, VA 23681

Graham Candler[†]
University of Minnesota, Minneapolis, MN 55455

Roger Kimmel[‡]
Air Force Research Laboratory, 2130 8th St., WPAFB, OH 45433

Abstract

The Hypersonic International Flight Research and Experimentation (HIFiRE) 5 flight experiment by Air Force Research Laboratories and Australian Defense Science and Technology Organization is designed to provide in-flight boundary-layer transition data for a canonical 3D configuration at hypersonic Mach numbers. This paper outlines the progress, to date, on boundary layer stability analysis for the HIFiRE-5 flight configuration, as well as for selected test conditions from the wind tunnel experiments supporting the flight test. At flow conditions corresponding to the end of the test window, rather large values of linear amplification factor are predicted for both second mode (N>40) and crossflow (N>20) instabilities, strongly supporting the feasibility of first in-flight measurements of natural transition on a fully three-dimensional hypersonic configuration. Additional results highlight the rich mixture of instability mechanisms relevant to a large segment of the flight trajectory, as well as the effects of angle of attack and yaw angle on the predicted transition fronts for ground facility experiments at Mach 6.

1. Background

Due to its influence on surface heat transfer, skin-friction drag, and flow-separation characteristics, prediction of boundary layer transition constitutes an important aspect of hypersonic vehicle design. Laminar to turbulent transition over realistic vehicle surfaces is often caused by surface roughness of sufficiently large magnitude. However, when the surface is relatively smooth, the transition process is initiated by linear instabilities of the laminar boundary layer. Typically, the second (or Mack) mode instability dominates transition in 2D and axisymmetric boundary layers with hypersonic edge Mach numbers, although centrifugal (i.e., Gortler) instabilities may also come into play when the surface has concave curvature along the streamwise direction. Three-dimensional boundary layers involve the additional mechanisms of stationary and traveling modes of crossflow instability and, depending on the geometric configuration, may include the attachment line instability as well [1].

Regardless of the speed regime, linear stability correlations have been quite successful in predicting the onset of transition when a single instability mechanism dominates the transition process [2]. Mixed mode transition has been more challenging to predict because of possible nonlinear interactions between the relevant modes of instability. To account for the effect of such interactions, an *ad hoc* composite metric based on the linear amplification factors for the different instability mechanisms has sometimes been used for transition correlation (see, for instance, [3]). Recent work on crossflow instability in low-speed boundary layers [4] has exposed additional shortcomings in applying purely linear predictive models to crossflow dominated transition in 3D boundary layers.

The simplest canonical configuration that includes the necessary elements for studying both mixed mode transition and crossflow evolution in the context of a hypersonic boundary-layer flow is a circular cone at small but nonzero angle of attack [5, 6]. Even though a number of experimental studies pertaining to circular cone transition under nonzero angle of incidence have been reported in the literature, a majority of this data was obtained in conventional (i.e., noisy) ground facilities and, moreover, is limited to the windward and leeward rays of symmetry. The observed trends are often paradoxical and have not been fully explained via boundary-layer stability analysis. An alternative canonical configuration involving a fully 3D surface geometry corresponds to an elliptic cone, which

---

was studied in detail by Kimmel and coworkers [7,8] via measurements in a conventional (i.e., noisy) wind tunnel and linear stability analysis.   The only extant data point involving in-flight measurements of crossflow transition in high-speed boundary layers corresponds to the Pegasus flight experiment [1].

The availability of quiet hypersonic facilities and measurement techniques enabling global imaging of transition fronts has opened the door to more comprehensive studies of transition characteristics in 3D boundary layers over smooth and rough surfaces. As an example, fundamental studies involving quiet tunnel measurements and analysis of crossflow induced transition on a circular cone at angle of attack to a Mach 6 free stream have recently been initiated [9, 10]. More importantly, activities under the Hypersonic International Flight Research Experimentation (HIFiRE) program are expected to provide boundary layer transition data for canonical hypersonic configurations under a variety of disturbance environments, including conventional and quiet facilities and high altitude flight. Such multi-pronged investigations should provide valuable insights into the effect of disturbance environment on hypersonic transition over 3D bodies and also facilitate complimentary measurements of the transition process in the different facilities.

The HIFiRE program is a hypersonic flight test program executed by the Air Force Research Laboratory (AFRL) and the Australian Defence Science and Technology Organization (DSTO) [11, 12]. Its purpose is to develop and validate technologies critical to the realization of next generation hypersonic aerospace systems. Candidate technology areas include, but are not limited to, propulsion, propulsion-airframe integration, aerodynamics and aerothermodynamics, high temperature materials and structures, thermal management strategies, guidance, navigation, and control, sensors, and weapon system components such as munitions, submunitions, avionics, and weapon system separation.

Two HIFiRE flights are devoted to boundary layer transition measurement. The primary experiment on HIFiRE-1 was devoted to laminar-turbulent transition on a circular cone at zero angle of attack.[11–18]. The objective of the HIFiRE-1 experiment was to examine second-mode transition. The HIFiRE-5 transition experiment extends the HIFiRE-1 effort to fully three-dimensional boundary layers, by seeking to transition locations around the body of a non-ablating, 2:1 elliptic cone. The experiment is designed to generate both crossflow and second-mode transition.

The primary goal behind the current work is to generate design data for HIFiRE-5. In particular, the transition behavior of the test article must be predicted near the beginning and end of the nominal test window to ensure that smooth-body transition will be observed during the flight. The application of modern parabolized stability equation (PSE) methods also permits a critical reexamination of the earlier linear stability results obtained for elliptic cones, as well as augmenting the severely limited knowledge base in applying such methods to fully three-dimensional boundary layers. The present paper provides a progress report on the ongoing analysis targeting these objectives.

2. HIFiRE-5 Experiment

The HIFiRE-5 concept configuration consists of an S-30 first stage [19] and Improved Orion [20] second stage, shown in Fig. 2.1. The S-30 / Orion stack will boost the test article to approximately 270 km, with a peak reentry Mach number of 7.5. The test article consists of a blunt-nosed elliptic cone of 2:1 ellipticity, 0.86 meters in length. Figure 2.2 presents a dimensioned drawing of the test article concept. The minor axis of the cone is a seven-degree half-angle. The nose tip cross-section in the minor axis describes a 2.5 mm radius circular arc, tangent to the cone ray describing the minor axis, and retains a 2:1 elliptical cross-section to the tip. Therefore, the model contour along any given meridian involves a curvature discontinuity at the juncture between the nose and the downstream cone portion. The cone is 431.8 mm wide at its base and overhangs the 355.6 mm diameter booster in the yaw plane. An uninstrumented section blends the elliptical cone cross-section into the circular booster cross section. Small canards for material tests may be incorporated onto the transition section. A cylindrical can containing GPS, antennas and other equipment resides between the transition section and the Orion booster. The vehicle is stable in yaw and pitch planes, and no shroud is currently envisioned. The payload does not separate from the second-stage Orion, and remains attached to it throughout the reentry. The vehicle is spin-stabilized. Cant-angle on the first and second-stage fins causes the vehicle to spin passively. Because of this, the payload is rolling at a very slow rate throughout the ascent and descent.

The entire reentry vehicle (payload plus second stage) is aerodynamically stable and will self-orient into a nose-first attitude during reentry upon achieving sufficient dynamic pressure. A cold-gas jet reaction control system aligns the vehicle during exoatmospheric flight so the vehicle longitudinal axis is approximately coincident with the reentry flight path vector. In this way the vehicle is at low angle of attack at the beginning of the test window, minimizing AOA oscillations during reentry and maximizing test time.

The vehicle will telemeter data constantly throughout reentry, but the beginning of the useful test window is defined by the altitude where the Reynolds number begins to be high enough to provide meaningful data. As a point

of reference, this is taken as h=36 km where the elliptic cone length Reynolds number reaches 1×10^6. Previous flight tests indicate that the vehicle departs from stable flight at about h=18-23 km, probably due to failure of the second-stage fins. This departure defines the end of the test window. The test window duration from h=36 km to h=18 km is approximately nine seconds.

The elliptic cone configuration was chosen based on past ground test and CFD. During the mid-1990s, several researchers investigated hypersonic transition phenomena on elliptic cones [21–28]. Investigators examined 4:1 and 2:1 elliptic cones. On the basis of this work, the 2:1 elliptic cone was chosen for the HIFiRE-5 configuration since it presents significant second-mode and crossflow instability and provides sufficient volume for instrumentation. Second-mode and crossflow instability are expected to be the dominant instability mechanism on maneuvering hypersonic vehicles.

Researchers conducted combined experimental and computational investigations of transition on a sharp-nose, 2:1 elliptic cone at Mach 8 [21-23]. The HIFiRE-5 geometry is identical to this configuration, except for the nose bluntness. 3D linear stability calculations using the E**Malik3D code revealed second mode instability and both traveling and stationary crossflow instability. Experiments in the Arnold Engineering Center von Karman Facility (AEDC VKF) Tunnel B did not reveal unequivocal evidence of stationary crossflow instabilities. It was speculated that background wind tunnel noise produced jitter in any stationary crossflow vortices, causing their heat transfer signals to wash out. Hot film probe measurements however, did indicate spectral content in the frequency range predicted for traveling crossflow instability. Additional spectral content was noted at higher frequencies corresponding to second-mode instabilities. Basic state computations indicated a thick, inflected boundary layer profile on the centerline (minor axis). Linear stability theory confirmed that this portion of the boundary layer was unstable to traveling instabilities and prone to early transition, and this was borne out by the AEDC tests. Centerline transition occurred at a length Reynolds number of approximately 5×10^5. The model leading edge (major axis), in contrast, was highly stable and remained laminar up to $Re = 5\times10^6$.

Wind tunnel experiments in support of the HIFiRE-5 flight test have recently been performed on 0.381 scale model in the 20 Inch Mach 6 wind tunnel at NASA Langley Research Center. The phosphor thermography images obtained in these tests provide global transition data over the cone surface. Measurements have been performed for both natural transition and transition in the presence of artificial trips mounted just aft of the nose. Quiet tunnel measurements on a cone model of the same scale are being performed by Prof. Schneider and his students at Purdue University. Additional data on a full scale model is being acquired in the conventional hypersonic facilities at Calspan-University of Buffalo Research Center (CUBRC).

3. Flow Conditions and Analysis Codes

To provide a basic state for the prediction of disturbance amplification characteristics, mean flow computations were carried out for a select set of flow conditions (Table 1), which included two points along the planned flight trajectory and other representative test conditions from the experiments at NASA Langley Research Center and Purdue University.

Both of the flight conditions from Table 1 correspond to approximately same Mach number (for simplicity, set equal to M=7 during the analysis) but sufficiently different altitudes (h = 18 km and h = 33 km, respectively) so as to bracket a large part of the test window that may be relevant to natural transition. The wind tunnel conditions are chosen to allow comparison with tunnel measurements, provide guidance for wind tunnel experiment, and capture off-design transition behavior at nonzero angle of attack or yaw (i.e., side slip) angle.

For both flight trajectory locations, the temperature distribution over the model surface was computed using 3D thermal analysis. However, the mean flow computations for the h = 18 km case were done using an earlier temperature estimate that was based on an axisymmetric heating model for a shrouded vehicle using a HIFiRE-1 trajectory. For that case, surface temperature near the nose is approximately 1400 K, and varies between 300 K and 400 K over much of the aft surface of the test article. Nose temperature for the higher altitude (h = 33 km) case is significantly lower, approximately 650 K. In the case of NASA LARC experiments, surface temperatures along the wind tunnel model were estimated from measurements along the geometric planes of symmetry. For the Purdue experiments, the entire model surface was assumed to be at $T_w = 300$ K.

The mean flow computations were performed using three different, state-of-the-art, compressible Navier-Stokes solvers. A majority of the mean flows were computed using the structured grid code LAURA (version A_1.2) from NASA Langley Research Center [29]. However, the unstructured grid solver US3D [30] played a central role during the feasibility analysis based on the flight conditions at h = 18 km. An additional structured grid solver, VULCAN (v. 6.0.2) [31], was also used in a small number of cases to provide code to code comparison. All three solvers use an effectively second order accurate spatial discretization based on a hexahedral grid. Throughout the computations, special care was exercised to ensure an appropriate resolution of the boundary layer flow while

maintaining a close alignment of the outer grid with the 3D shock surface. The computed basic state was fully laminar with the assumption of ideal gas behavior; no turbulence model or real-gas approximations were included in these computations.

Table 1. Flow Conditions Selected for Computations

Case designation	Case description	Section in paper outlining results for this case	Altitude h (km)	M_∞	α (deg)	β (deg)	T_∞ (K)	ρ_∞ (kg/m^3)	Nominal Unit Re (Million/ft)
Flt18km	Flight – High Re	4A	18	7	0	0	216.65	0.1267	5.63
Flt33km	Flight – Low Re	4B	33	7	0	0	230.97	0.01157	0.503
PUa0b0R3	0.381 scale model tested in quiet facility at Purdue University	5A	N/A	6	0	0	52.8	0.04034	3.0
PUa4b0R3		5C		6	4	0	52.8	0.04034	3.0
LARCa0b0R5	0.381 scale model tested in LARC 20 Inch Mach 6 Tunnel	5B		6	0	0	62.4	0.08298	5.3
LARCa4b0R4		5D		6	4	0	62.0	0.06178	4.1
LARCa0b4R6		5E		6	0	4	63.2	0.08745	5.6

The relevant flow symmetries were exploited to restrict the computational domain accordingly. For the baseline vehicle attitude corresponding to $\alpha = \beta = 0$, the computational domain included just one quarter of the total body surface. Similarly, for nonzero α or β (but not both nonzero simultaneously), only one half of the body surface was gridded for the computations. The grid topology was effectively equivalent to a structured grid consisting of two blocks, one near the nose and a second one that covered most of the body length downstream of the nose. Typically, the downstream block was discretized using 250 to 341 points in the streamwise (ξ) direction, 181 points (361 points for the half body computations at $\alpha > 0$ or $\beta > 0$) in the azimuthal (θ) direction, and 300 to 351 points in the surface normal (η) direction. For grid convergence studies, additional computations were done using twice the number of points in a given direction (but not multiple directions at the same time). The grid was suitably clustered in all three computational coordinates. The boundary conditions employed during the mean flow computations were typical of blunt body computations involving one or two planes of symmetry and a nonsingular grid over the nose region.

The stability of the 3D boundary layer flow is analyzed using the Langley Stability and Transition Analysis Code (LASTRAC) [16]. Analysis is performed using both 1D and 2D (i.e., planar) stability theory and the parabolized stability equations (PSE). For the purpose of stability analysis, the computed mean flow is interpolated to a grid that is better suited for stability analysis. Grid convergence relative to the stability grid was assessed via spot checks for different type of instabilities. Sutherland's law is assumed to describe the viscosity variation for both mean flow and instability induced perturbations. Stoke's hypothesis is assumed for the bulk viscosity.

We note that the boundary layer flow over the HIFiRE-5 configuration varies along both coordinate directions spanning the test surface. This lack of flow homogeneity along both surface coordinates leads to both fundamental and practical challenges for the linear stability theory and its application to transition prediction using the N-factor methods [33–35]. In particular, the modal ansatz for the perturbation field, which decouples the various length scales (i.e., Fourier modes) along the homogeneous flow direction, is not applicable to fully 3D boundary layers and,

strictly speaking, the disturbance evolution characteristics depend upon the details of the spatial distribution of unstable perturbations at a suitable upstream location.

Even though a local modal ansatz may be justified under the framework of classical stability theory for weakly non-parallel mean flows, further assumptions are necessary to both define a closed eigenvalue problem for 3D disturbances and to use the computed eigenvalues towards transition correlations based on the linear amplification ratio (i.e., N factor). In particular, the fact that the disturbance amplitudes evolve in both directions along the body surface makes it essential to invoke additional (and typically ad hoc) approximations in order to select an appropriate trajectory for the integration of disturbance amplification rates.

The effectiveness of quasi-parallel analyses based on linear stability theory can only be justified via extensive comparisons against sufficiently detailed experimental measurements, and/or theoretical or numerical methods that include the effects of boundary layer growth and mean flow variations along both surface coordinates. For example, encouraging comparison with measured transition fronts has been demonstrated in a few select cases [36–38]. Several non-parallel procedures based on parabolized stability equations (PSE), all of them involving implicit assumptions about the disturbance initiation process, have also been described in the literature [32, 39, 40].

As a result of the *ad hoc* decisions inherent to applying linear stability correlations to fully 3D flows and the limited pertinent knowledge base especially for hypersonic flows, the current effort applies a judicious mix of methods with varying degrees of approximations, so that the conclusions are not based on a single method alone. A majority of the results are based on quasi-parallel theory with curvature effects taken into account. Higher fidelity methods are used, as necessary, to quantify the effects of mean-flow non-parallelism. In general, the amplification potential of unstable disturbances is quantified by integrating the disturbance growth along streamline trajectories, although limited results are also obtained with group velocity trajectories. Due to the amount of effort involved, a thorough analysis has not been completed as yet. However, the salient features of instability characteristics in the selected cases are highlighted below in Section IV.

4. Instability Characteristics at Flight Conditions
A. Case Flt18km: Flight condition, h = 18 km

Results for the h = 18 km flight condition are considered first. Because this condition corresponds to the highest flow Reynolds number during the test window, confirming a high probability of transition in this case was essential to establishing the feasibility of the experiment. In addition, computations for this case were also beneficial in identifying the frequency bandwidth needed by the surface instrumentation for measuring the traveling crossflow modes. Figure 4.1 outlines the overall behavior of the boundary layer flow over the HIFiRE-5 test surface at $\alpha = \beta = 0$. Limiting surface streamlines based on the surface shear stress distribution (Fig. 4.1a) illustrate the azimuthal movement of the boundary layer flow towards the vertical plane of symmetry, i.e., the minor axis plane y=0. The inclination of the skin friction lines (Fig. 4.1a) relative to the inviscid streamlines near the edge of the boundary layer (Fig. 4.1b) indicates the presence of strong crossflow inside the boundary layer. The inward directed crossflow (together with a lack of sufficient acceleration along the streamwise direction) leads to a substantial thickening of the boundary layer near the y=0 plane as seen from the axial velocity contours at selected *x* locations (Fig. 4.1c). Similar flow behavior was noted earlier in the context of a sharp nosed model [23].

Surface distributions of transition relevant mean-flow parameters are shown in Figs. 4.2a through 4.2c. In particular, Fig. 4.2a shows the distribution of Re_θ/M_e (where Re_θ denotes the momentum thickness Reynolds number and M_e represents the flow Mach number at the edge of the boundary layer) over the cone surface. Analogous distribution of the crossflow Reynolds number R_{cf} is shown in Fig. 4.2b. The maximum crossflow velocities occur near $y/y_{max} \approx 0.75$; however, the maximum values of the crossflow Reynolds number occur further inboard, i.e., relatively closer to the minor axis plane (y=0). The reason behind this particular trend is attributed to the thickening of the boundary layer as the minor axis plane is approached (Fig. 4.1c). The shape of the Re_θ/M_e contours in Fig. 4.2a is quite similar to that of the R_{cf} contours in Fig. 4.2b, with the peak values of Re_θ/M_e occurring somewhat outboard of the vertical plane of symmetry. The variation of the attachment line Reynolds number along the length of the leading edge (i.e., along the z=0 meridian of symmetry, where the flow bifurcates between the top and bottom portions of the body) is shown in Fig. 4.2c. Based on the approximate mean flow correlations for transition onset (see, for instance, ref. [1, 28]), the values of all three Reynolds number parameters from Figs. 4.2a−4.2c are large enough that the onset of transition due to either one or more of the instability mechanisms involving streamwise, crossflow, and attachment line instabilities is deemed to be almost certain at the trajectory point of interest.

The linear stability characteristics of the mean flow described above are examined next. Figures 4.3a through 4.3c, respectively, display the contours of integrated amplification ratio (i.e., N factor) for streamwise, stationary crossflow and traveling crossflow instabilities over the surface of the test article. There is strong amplification of

2D instability modes along both major and minor axis planes of symmetry, and the crossflow instability dominates in the middle.

Consistent with the large values of R_{cf} in Fig. 4.2b, the N factor values for crossflow instability are also large in comparison with typical N-factor correlations for transition onset in low disturbance environments [1]. The maximum N-factor based on the integration of peak amplification rate (locally maximized over all spanwise wavelengths at a fixed frequency) along streamline trajectories is already larger than N=20 at x=0.6 m and continues to increase at farther downstream locations. N-factor distribution obtained by tracking individual stationary modes of constant wavelength is very similar as well, and the most amplified stationary modes correspond to a wavelength of approximately 2 mm in the direction that is normal to the local inviscid streamline. It may be noted that the range of N-factors correlating with transition onset via stationary crossflow modes may vary considerably depending on the surface roughness characteristics. However, the likelihood of transition not occurring over a nominally smooth aerodynamic surface in the light of such large N-factor values would appear to be small. Recall that, for the Pegasus wing glove experiment [1], transition locations based on thermocouple data from both the glove and the adjacent tile regions were found to correlate with stationary-crossflow N-factors within the range of 7 to 12.4 and with traveling mode N-factors between 7.6 and 14.1.

The N-factor distribution for the traveling modes of crossflow instability is qualitatively similar to those plotted in Fig. 4.3b for the stationary modes, except that the corresponding N-factors are somewhat larger. The approximate frequency range corresponding to peak amplification ratios corresponds to 10 kHz to 30 kHz; however, this peak is rather broad and, therefore, significant disturbance growth is also predicted at frequencies that are lower or somewhat higher than the above range. Overall, these traveling crossflow modes should be amenable to in-flight measurements using surface mounted instrumentation.

Details of the instability analysis along the attachment line (i.e., the model leading edge or the major axis plane z=0) are shown in Fig. 4.4. The attachment line velocity profiles are non-inflectional in this case and, therefore, the observed instability modes are connected to the acoustic family of modes which owe their existence to the region of relative supersonic flow inside the boundary layer [33]. The N-factor values for 2D disturbances are seen to exceed N=30 at x=0.6 m, indicating a strong likelihood of transition along the attachment line. The disturbance frequencies for these instability modes are in the mega-Hertz range (i.e., beyond the range of planned HIFiRE-5 instrumentation) — the most amplified disturbance at x = 0.8 m corresponds to a frequency of around 2 MHz, whereas the dominant frequencies at x = 0.2 m are seen to approach 4 MHz.

Previous studies [41, 42] for subsonic and low-supersonic boundary layers have shown that additional modes of attachment line instability can arise when the mean flow divergence on either side of the attachment line has been accounted for via a planar (i.e., 2D) eigenvalue analysis. These additional modes were shown to bifurcate from the conventional, Gortler-Hammerlin mode or, alternatively, the Hall-Malik-Poll mode [43], which had a first-mode like character for the cases studied in the previous works. Since the combination of higher Mach number and strong wall cooling leads to a different instability mechanism (namely, acoustic mode instability) in the present case, eigenvalue analysis based on a planar (i.e., 2D) partial differential equation (PDE) was performed to investigate the likely existence of higher modes in the vicinity of the HIFiRE-5 attachment line. Analysis at x = 0.4 m revealed that higher modes do, indeed exist in this case as well; but, similar to the lower-Mach-number studies [41, 42], these higher modes have lower growth rates in comparison with the (only) mode predicted via the conventional (i.e., 1D or ordinary-differential-equation based) instability analysis in Fig. 4.4.

The highest N factors over the model surface are predicted to occur in the vicinity of the minor axis plane of symmetry, i.e., along the y=0 meridian. N-factor curves for 2D disturbances[§] over a range of frequencies are shown in Fig. 4.5a. The instability growth characteristics along the y = 0 meridian are considerably different from those along the attachment line (Fig. 4.4a). Whereas the attachment line disturbances were dominated by classical second mode instabilities, each of which amplifies over a small portion of the body length, the boundary layer flow along the minor axis plane of symmetry exhibits a broader variety of disturbance modes. The dominant modes undergo a sustained amplification over much of the body length and correspond to a frequency range of approximately 250 kHz to 350 kHz (Fig. 4.5b). These modes exhibit three separate peaks in growth rate distribution along the length of the body. During the course of this 3-lobe amplification, the modal character appears to switch seamlessly from a supersonic mode (centered around the first valley in growth rate distribution) to 2nd mode and, eventually, to what might be called a shear layer mode, because of its concentration within the region of high shear well away from the

---

[§] In this paper, the phrase "2D disturbance" denotes a disturbance entity with its wavenumber vector aligned with the inviscid flow direction. This is to be distinguished from "2D eigenvalue analysis" which refers to eigenvalue analysis based on the discretization of a planar (i.e., 2 dimensional) partial differential equation, as against the conventional "1D analysis" as discussed in the context of Fig. 4.4.

surface (Fig. 4.6a–c). The progressive development of this region of high shear along the axial direction was shown previously in Fig. 4.1c. .

The boundary layer flow along the y=0 meridian also supports oblique (i.e., 3D) instability modes with a nonzero wavenumber normal to this meridian. Figures 4.7a and 4.7.b show the N factors and wave angles versus x for first mode disturbances with f = 20-250 kHz obtained by maximizing the growth rate at each streamwise location. Lower frequency (20-200 kHz) disturbances shown here are clearly predominantly first mode, because the corresponding wave angles are in the range of 10-75 degree across the whole x range. Higher frequency disturbances are mixed first- and second-modes because the most unstable mode is oblique for x < 0.6 and becomes 2D beyond that. The resulting N factor for higher frequency disturbances also approach that of pure second modes shown in Fig. 4.5a. Given the cold surface temperatures under the flight conditions ($T_w/T_{a,w} < 0.3$ over most of the cone surface downstream of the nose), it is somewhat surprising to observe first mode like instabilities in the present case. For a flat plate boundary layer, the same cold wall condition would have stabilized or almost stabilized the first mode disturbances. A likely cause for the destabilization of first mode disturbances may be related to the highly inflectional character of the mean flow profiles along the y=0 meridian. As noted in the context of Fig. 4.6, the modified cold-wall boundary layer has shear layer characteristics and this may lead to reduced sensitivity to wall cooling.

Because of the enhanced significance of azimuthal mean flow gradients in the vicinity of the boundary layer bulge along y=0, it is useful to examine their effect on the instability modes in this region. Mode shapes obtained via a 2D eigenvalue analysis at a selected axial location and disturbance frequency are shown in Fig. 4.8. Similar to the attachment line (z=0) analysis in Fig. 4.4b, results from the 2D eigenvalue analysis near y=0 also indicate the potential for additional instability modes; the peak fluctuations associated with these modes are concentrated within separate regions of high basic state shear in the vicinity of the y=0 plane. Such intricacies of the instability characteristics in the vicinity of the minor axis plane of symmetry also indicate the need to exercise caution in using stability analysis along the symmetry plane alone to draw inferences regarding the growth of unstable perturbations in the vicinity of this plane.

An alternative way to account for the effect of azimuthal variations in the basic state corresponds to surface marching PSE [32]. Predictions based on surface marching PSE analysis are shown in Fig. 4.9, which displays the contours of linear amplification ratio for a disturbance of fixed frequency (f = 400 kHz) that is initiated with uniform amplitude distribution at a suitably chosen upstream location. The uniform initial amplitude is used as a reference to normalize the computed disturbance amplitudes at the downstream locations, so as to express their evolution in terms of an N-factor distribution. The large values of N-factors computed in this manner provide an additional confirmation of the previous conclusion concerning an almost certain onset of laminar-turbulent transition over the test surface at the h = 18 km trajectory point. Further computational work is currently under way to provide more in depth comparisons between the various prediction techniques as well as to obtain additional insights towards the application of such advanced techniques towards transition prediction for fully 3D flows.

Following the completion of the stability analysis outlined above, additional mean flow solutions for the same case were also obtained using the LAURA [29] and VULCAN [31] codes. The computational grids used for the latter calculations provided significantly higher resolution of the boundary-layer flow, as well as allowing an assessment of grid convergence of the mean flow solutions. The LAURA solutions showed, in particular, that the details of the boundary-layer flow near the minor axis plane of symmetry were sensitive to grid resolution (especially for this high Reynolds number case) as well as to code-to-code differences, but the profiles over the rest of the model surface were virtually invariant with respect to further refinements in the gird. Because of the need to extend the stability analysis to other flow conditions, a detailed stability analysis using the LAURA and VULCAN solutions has not been repeated yet. However, computations of stationary crossflow instability using one of the LAURA solutions showed similar distribution and values of N factors as those obtained using the US3D mean flow solution. An analogous scrutiny for the more sensitive region near the y=0 plane is deferred to the follow-on effort to this paper. The mean flow solutions for the remaining cases described below were based on the LAURA computations.

B. Case Flt33km: Flight condition, h = 33 km

The unit Reynolds number for this high altitude case is approximately 11 times smaller than the Reynolds number for the h = 18 km case described in Section 4A. Consistent with the lower Reynolds number, the secondary flow roll-up near the minor axis plane of symmetry is weaker than that encountered previously for the h = 18 km trajectory point (Fig. 4.1c). The overall N-factors for both second mode and crossflow instabilities are also considerably lower in comparison with the h = 18 km case. N-factor values in the vicinity of the y=0 line were found to be marginal for transition in a flight environment, but no definitive conclusion could be drawn due to the

increased complexity of the basic flow in this region. No significantly strong first mode instability was detected along either meridian of symmetry.

Peak value of the N-factor for stationary crossflow modes is approximately 5 or less and, roughly speaking, the locus of peak N-factors at each axial station bisects the body surface as viewed along the z-axis (Fig. 4.10). As seen from the comparison of Figs. (4.10a) and (4.10b), the N-factor distributions based on mode tracking with constant circumferential mode number and an envelope method, respectively, are close to each other. The low values of peak N-factor in these figures indicate that transition due to stationary crossflow modes is unlikely at the h = 33 km condition, assuming that the surface finish of the test article is comparable to or better in comparison with the surface finish used in typical laminar-flow applications at comparable Reynolds numbers. A similar conclusion regarding the onset of transition was also reached on the basis of instability analysis for the traveling crossflow modes.

5. Instability Characteristics at Selected Wind Tunnel Conditions

In terms of cone length Reynolds number, the wind tunnel cases from Table 1 fall in between the two flight conditions considered in Section 4. However, these wind tunnel cases differ from the flight trajectory conditions in two important respects, namely a lower free-stream Mach number (M=6 vs. M=7 for the flight conditions) and significantly larger values of the T_w/T_{aw} ratio. For example, the wall temperature ratio along the leading edge (i.e., the attachment line) over the aft surface of the wind tunnel models is within the range of 0.7 to 0.8, as against 0.15 to 0.25 under the flight conditions. Due to these differences, the first mode instabilities would be somewhat stronger in comparison with those encountered on the flight article at the same body-length Reynolds number and, therefore, could become significant, especially at higher Reynolds numbers.

A. Case PUa0b0R3: Purdue Quiet Tunnel, $\alpha=0$, $\beta=0$, Re=3M/ft

Fig. 5.1 shows the predicted heat flux distribution over the body surface, along with axial velocity contours at selected x locations. The warm and cool streaks outboard of the y=0 meridian appear to correlate, respectively, with the thinning and thickening of the velocity boundary layer along the azimuthal direction.

N-factor distributions for 2D, streamwise instabilities are shown in Fig. 5.2a. Peak N-factors slightly outboard of the y=0 symmetry line are larger than those at the symmetry line itself. However, given the complex structure of the mean flow in this region, coupled with the non-uniqueness of defining an integration trajectory for N-factor calculation, the results of this figure should be best interpreted as bounding the range of N-factors within the region of bulge in the mean boundary layer thickness. Effect of mean-flow non-parallelism on disturbance amplification along the y=0 plane are shown in Fig. 5.2b. The differential in N-factor values based on quasi-parallel linear stability theory (denoted as LST in the figure legend) and parabolized stability equations (PSE) is seen to be approximately 1 in the case of the most amplified frequency.

Figures 5.3a through 5.3d illustrate the N-factor distribution for stationary crossflow modes, as computed using different possible options for growth rate integration. The corresponding N-factor curves for a select set of integration trajectories are shown in Figs. 5.4a through 5.4d, respectively. Visually, all four methods yield very similar N-factor distributions, with the maximum discrepancy among the respective predictions of peak N-factor over the model surface being approximately equal to 2. Furthermore, the N-factor predictions based, respectively, upon growth rate maximization over β and mode tracking for fixed circumferential mode number m_β appear to be rather close to each other. Analogously, the remaining two methods (based on mode tracking for constant β and maximized growth rate along group velocity trajectory) appear to yield rather similar predictions as each other. Overall, the N-factor values in Figs. 5.3 and 5.4 are such that transition due to stationary crossflow modes alone would be a finite possibility depending on the surface finish characteristics of the model.

Effects of mean-flow non-parallelism on disturbance amplification along a selected integration trajectory (within the region of peak N factors) are shown in Figs. 5.5a and 5.5b. Typical of crossflow instability, in general, non-parallel effects are moderately destabilizing, resulting in the PSE-based peak N-factor being larger then the quasi-parallel (QPWC) prediction by approximately 1.

The N-factor distribution based on traveling crossflow modes is shown in Fig. 5.6a. The peak N factor for traveling crossflow modes is larger than the corresponding value for stationary modes in Fig. 5.3a by approximately 4 to 5. Furthermore, the locus of peak N-factors for the traveling crossflow modes appears to be slightly farther inboard (i.e., closer to the y=0 axis) in comparison with the analogous locus for stationary crossflow modes. The highest N-factors correspond to traveling crossflow modes near f=35–40kHz. To help determine whether or not the traveling crossflow modes could also be detected via surface instrumentation, Fig. 5.6b Shows the magnitude of pressure eigenfunctions (scaled by two times the local dynamic pressure) at selected x locations along a particular

integration trajectory within the region of dominant crossflow growth. For a unit amplitude peak temperature perturbation associated with the traveling crossflow modes, the highest non-dimensional surface pressure fluctuations occur along the upstream part of the trajectory and decrease nearly 7 times from x = 0.05m to x = 0.3m.

B. Case LARCa0b0R5 (NASA LARC, M=6, α=0, β=0, Re=5.3M/ft)

Figures 5.7a and 5.7b display overall distributions of the N-factors for 2D streamwise and traveling crossflow modes, respectively. Since the peak N factors exceed 20 in both cases, transition via either mode of instability is very likely at this wind tunnel condition.

To assess the non-parallel effects on disturbance evolution in this case, linear PSE analyses were carried out at three selected marching paths (see Fig. 5.8) that collectively exhibit the amplification characteristics of all relevant disturbance modes, namely, streamwise modes (including first mode, second mode, and the accompanying shear layer modes), crossflow disturbances, and instability modes near the attachment line. Hereafter, the N factors computed by tracking individual instability modes corresponding to specified combinations of disturbance frequency and spanwise wave number using linear PSE are compared with those obtained using quasi-parallel linear stability theory with both streamwise and spanwise curvature terms accounted for (QPWC). Note that these parallel N factors are different from those shown in Fig. 5.7b, which were obtained by integrating the maximized growth rate at each location using the envelope method. Along the y = 0 meridian, the overall N factors at the end of the domain change from QPWC values of 12 and 12.4 for first- and second-mode instabilities, respectively, to linear PSE values of 12.3 and 11.2.   Because of the bulge in the boundary layer thickness along the symmetry line, the second mode disturbances here are in fact, shear layers instability modes. Based on the maximum N-factor envelopes, the middle streamline shown in Fig. 5.7b falls within the region of largest crossflow disturbance growth. For this integration trajectory, the overall N factors obtained from individual mode tracking for stationary and traveling crossflow disturbances increase from QPWC values of 12 and 16.2 to linear PSE values of approximately 13.3 and 19, respectively.

Computational results along the attachment line (z=0) show negligible non-parallel effects on the second-mode disturbances. However, the linear PSE N factor for oblique first-mode instability waves is much larger than that obtained from QPWC. As shown in Fig. 5.8b, the overall N factor increases from 3.2 to 10.6. Both QPWC and linear PSE results shown here were calculated by tracking modes with a specific disturbance frequency and spanwise wave length.   Such significant non-parallel effect might be attributed, in part, to the fast divergence of the geometry (due to increasing cone dimension along the downstream direction) and the large curvature around the attachment line boundary layer. For a divergent geometry such as a circular or elliptic cone, integrating the disturbance growth by tracking modes with a constant spanwise wavelength may not reflect the true flow physics because of the periodicity constraint of waves around the circumference. Alternatively, one can integrate modes with a constant, integer azimuthal wave number with the integer value indicating the total number of waves around the circumference of the local cross section. Figure 5.8c shows the same comparison between QPWC and linear PSE obtained by varying the azimuthal wave number from 90 to 260.   The azimuthal wave number is held constant at all streamwise locations in these calculations. The overall N factor now becomes 3.1 and 6.6 for QPWC and linear PSE, respectively. While the change for QPWC is minimal, PSE N factor is substantially smaller with the constant azimuthal wave number approach. The increase of N factor from 3.1 to 6.6, even though larger than previously shown cases, is more in line with that observed in axisymmetric configurations. More advanced stability analyses such as a DNS and/or plane-marching PSE method will be used in future to help verify the magnitude of this discrepancy as well as whether the constant-azimuthal-wave-number PSE approach is indeed more accurate.

Except for the attachment line, effects of mean-flow non-parallelism are similar to past experience with similar instability mechanisms in either 2D or infinite swept boundary layers. Transition locations based on phosphor thermography images acquired during the NASA LARC wind tunnel experiments were estimated to be near *x* = 0.088 m to 0.091 m along the minor axis symmetry plane, *x* = 0.095 m ~ 0.097 m along the middle streamline, and *x* = 0.256 m along the attachment line (or the major axis plane of symmetry). At these locations, transition N factors correlated with the various instability mechanisms are summarized in Table 2. These transition N values, i.e., around 2 to 3 for first- and second-mode disturbances and around 4 for stationary and 6 ~ 7 for traveling crossflow instability waves, are somewhat low compared to previous experiments. For the attachment line boundary layer, using constant azimuthal wave number gives a lower, and perhaps more reasonable, N value of 5.22 for linear PSE. However, it should be noted that the cause for transition along the attachment line cannot always be readily inferred from the thermography image.

Table 2 Comparison of transition N-factors at three integration paths

Integration Trajectory (Measured Transition Location)	N-factor (disturbance frequency)			
	First Mode (QPWC)	Second Mode (QPWC)	First Mode (PSE)	Second Mode (PSE)
Minor Axis, y=0 (x_{tr} = 0.09 m)	1.89 (40 *kHz*)	1.84 (170 *kHz*)	2.97 (40 *kHz*)	2.03 (170 *kHz*)
Major Axis, z=0, i.e., Attachment Line (x_{tr} = 0.256 m)	2.48 (90 *kHz*) 2.17 (n = 90)	3.29 (1.1 *MHz*)	8.3 (130 *kHz*) 5.22 (n = 110)	3.30 (1.1 *MHz*)

Integration Trajectory (Measured Transition Location)	N-factor (disturbance frequency)			
	Stationary Crossflow (QPWC)	Traveling Crossflow (QPWC)	Stationary Crossflow (PSE)	Traveling Crossflow (PSE)
Middle Streamline (x_{tr} = 0.096 m)	4.34 (0.8 *mm*)	6.04 (90 *kHz*)	4.55 (1.1 *mm*)	7.13 (90 *kHz*)

C. Effect of Angle of Attack and Yaw Angle

This final subsection outlines the effects of angle of attack and yaw angle on the transition front associated with stationary crossflow modes. Figs. 5.9a and 5.9b show the N-factor contours for cases PUa0b0R3 and PUa4b0R3, respectively (i.e., for the Purdue HIFiRE-5 model at α=0 and α=4 deg, respectively, at a unit Reynolds number of 3M/ft). Due to the lack of processed heat transfer data from the Purdue quiet tunnel experiments at this stage, the phosphor thermography data from the (conventional facility) NASA Langley experiments at approximately matching Reynolds number is also included in Fig. 5.9a. As seen during the previous sections in the context of the α=0 configuration, the predicted transition front based on the stationary crossflow modes alone consists of one lobe for each quadrant of the model cross-section. At α=0, the attachment line location coincides with the (geometric) major axis plane of symmetry and the crossflow transition lobe over each quadrant of the model surface corresponds to a mirror image of the adjacent two. A small, nonzero angle of attack causes the "attachment" line to deviate from the major axis plane of symmetry (z=0), resulting in different amounts of crossflow on the top (i.e., leeward) and bottom (i.e., windward) sides of the body surface. As may be expected, the thicker boundary layer on the leeward side supports substantially stronger crossflow instability, leading to higher N-factors than those for the baseline, zero angle-of-attack configuration. Therefore, crossflow induced transition would be expected to occur much earlier over the two surface quadrants on the leeward side. It should be noted that the 4-lobe topology of stationary crossflow N-factor distribution over the HIFiRE-5 model is intrinsically different from that over a slender circular cone at comparable angles of attack (Fig. 5.9c, which shows similar predictions for a 7-degree circular cone at 6 deg AOA in the Purdue Mach 6 tunnel [9, 10]).

On the other hand, for the α=0, β=4 deg configuration, the attachment line location remains fixed along the major axis plane of symmetry, as in the baseline case of α=β=0. However, as shown in Fig. 5.10a, the lateral asymmetry due to the yaw angle leads to a progressive departure in the location of boundary layer thickening (where the incoming crossflow from either side of the body collides with each other) from the minor axis plane of symmetry. The corresponding N-factors, shown in Fig. 5.10b, indicate stronger crossflow instability on the starboard side, with peak N-factors in excess of 20. N-factor values along the port side are smaller, so that transition may or may not be expected to occur on that side depending on the surface roughness environment.

6. Summary

Planned hypersonic flight experiments, along with the availability of quiet hypersonic facilities, have opened up the possibility of a detailed study of hypersonic transition phenomena for fully 3D configurations. These experiments must, however, be guided by a detailed analysis of the flow field and its instability characteristics. The objective of this ongoing effort has been to provide such characterization in support of the HIFiRE-5 flight experiment, and pave the way to address some of the outstanding issues related to transition prediction for fully 3D hypersonic flows and crossflow transition in hypersonic boundary layers in general. Initial results presented in this

paper confirm the feasibility of natural transition onset during the test window, as well as indicating a rich instability structure involving potential intermodal interactions. Potential intricacies of instability mechanisms near the minor axis plane of symmetries have been identified. The paper also outlined the first set of results involving 2D eigenvalue analysis of an attachment line boundary layer at hypersonic speeds; the findings indicate a similar hierarchy of the higher attachment line modes as that of the subsonic and supersonic boundary layers [18, 19], despite the fact that the underlying instability mechanism in the present case is of the second mode type, i.e., completely different from those operative in the slower speed regimes.

Limited comparison with conventional facility measurements confirmed qualitative similarity between the predicted N-factor contours and the transition fronts inferred from thermography images in conventional facility experiments at other test conditions. The correlating N-factors appear to be low and further work is under way to facilitate more reliable comparisons with the data. The follow-on effort under this ongoing analysis is focused on more thorough application of higher fidelity analysis tools and a deeper investigation of instability physics using numerical computations pertaining to both natural transition (see, for instance, Fig. 6.1) and the effect of boundary layer trips [44].

Acknowledgments

References

1. Malik, M., Li, F., and Choudhari, M., "Analysis of Crossflow Transition Flight Experiment aboard Pegasus Launch Vehicle," AIAA Paper 2007-4487, 2007.
2. Malik, M. R., "Prediction and Control of Transition in Supersonic and Hypersonic Boundary Layers," AIAA Journal, Vol. 27, No. 11, pp. 1487-1493, 1989
3. Schneider, S.P., "Design of a Mach-6 quiet-flow wind-tunnel nozzle using the e**N method for transition estimation," AIAA Paper 1998-547, 1998.
4. Saric, W.S., Reed, H.L., and White, E.B., "Stability and Transition of Three-Dimensional Boundary Layers," Ann. Rev. Fluid Mech., Vol. 35, pp. 413-40, 2003.
5. Schneider, S.P., "Hypersonic Laminar-Turbulent Transition on Circular Cones and Scramjet Forebodies," Prog. in Aerospace Sc., Vol. 40, pp. 1-5, 2004.
6. Stetson, K.F., Thompson, E.R., Donaldson, J.C., and Siler, L.G., "Laminar Boundary Layer Stability Experiments on a Cone at Mach 8 – part 3: Sharp Cone at Angle of Attack," AIAA Paper 85-0492, 1985.
7. Kimmel, R., "Laminar-Turbulent Transition in a Mach 8 Elliptic Cone Flow," AIAA J., Vol. 37, No. 9, pp. 1080-87, 1999.
8. Poggie, J. and Kimmel, R., "Traveling Instability Waves in a Mach 8 Flow over an Elliptic Cone," AIAA J., Vol. 38, No. 2, pp. 251-58, 2000.
9. Swanson, E., Ph. D. Dissertation, School of Aeronautics and Astronautics, Purdue University, 2008.
10. Choudhari, M., Chang, C.-L., Li, F., Edwards, J., and Candler, G., "Hypersonic Boundary Layer Transition: Roughness Effects and 3D Configurations," NASA Fundamental Aeronautics Program Annual Meeting, Atlanta, GA, Oct. 5-7, 2008 (Also: Choudhari, M., Chang, C.-L., White, J., and Li, F., "A Computational Study of Instability Excitation and Development in Hypersonic Boundary Layer over Circular Cone at Angle of Attack," to be submitted for publication).
11. Dolvin, D., "Hypersonic International Flight Research and Experimentation (HIFiRE) Fundamental Science and Technology Development Strategy," AIAA Paper 2008-2581, 2008.
12. Kimmel, R. L., Adamczak, D., Gaitonde, D., Rougeux, A., Hayes, J. R., "HIFiRE-1 Boundary Layer Transition Experiment Design," AIAA paper 2007-0534, January 2007.
13. Berger, K. T., Greened, F. A., Kimmel, R. L., Alba, C., and Johnson, H., "Aerothermodynamic Testing and Boundary-Layer Trip Sizing of the HIFiRe Flight 1 Vehicle," AIAA Journal of Spacecraft and Rockets, vol. 46, no., 2, March-April, 2009, pp. 473-480.
14. Kimmel, R. L., "Aerothermal Design for the HIFiRE-1 Flight Vehicle," AIAA Paper 2008-4034, June 2008.
15. Kimmel, R. L., "Roughness Considerations for the HIFiRE-1 Vehicle," AIAA Paper 2008-4293, June 2008.
16. Johnson, H. B., Alba, C. R., Candler, G. V., MacLean, M., Wadhams, T, and Holden, M. "Boundary Layer Stability Analysis of the Hypersonic International Flight Research Transition Experiments," AIAA Journal of Spacecraft and Rockets, vol. 45, no. 2, March-April 2008.
17. Alba, C. R., Johnson, H. B., Bartkowicz, M. D., and Candler, G. V., "Boundary-Layer Stability Calculations for the HIFiRE-1 Transition Experiment," AIAA Journal of Spacecraft and Rockets, vol. 45, no. 5, November-December 2008.

18. Wadhams, T. P., Mundy, E., MacLean, M. G., and Holden, M. S., "Ground Test Studies of the HIFiRE-1 Transition Experiment Part 1: Experimental Results," AIAA Journal of Spacecraft and Rockets, vol. 45, no. 6, November-December 2008, pp. 1134-1148.
19. Palmerio, A. F.: Peres da Silva, J. P. C.; Turner, P.; Jung, W., "The development of the VSB-30 sounding rocket vehicle," in 16th ESA Symposium on European Rocket and Balloon Programmes and Related Research, 2 - 5 June 2003. Ed.: Barbara Warmbein. ESA SP-530, Noordwijk: ESA Publications Division, 2003, p. 137 - 140
20. "NASA Sounding Rocket Program Handbook," 810-HB-SRP, Sounding Rockets Program Office, Suborbital & Special Orbital Projects Directorate, Goddard Space Flight Center, Wallops Island Flight Facility, June 2005.
21. Kimmel, R. L., and Poggie, J., "Transition on an Elliptic Cone at Mach 8," American Society of Mechanical Engineers ASME FEDSM97-3111, June 1997.
22. Kimmel, R. L., and Poggie, J., "Three-Dimensional Hypersonic Boundary Layer Stability and Transition," Air Force Research Laboratory Technical Report, WL-TR-97-3111, Wright-Patterson Air Force Base, Ohio, December 1997.
23. Kimmel, R. L., and Poggie, J., Schwoerke, S. N., "Laminar-Turbulent Transition in a Mach 8 Elliptic Cone Flow," AIAA Journal, vol. 37, no. 9, pp. 1080-1087, Sep. 1999.
24. Schmisseur, J. D., "Receptivity of the Boundary Layer on a Mach-4 Elliptic Cone to Laser-Generated Localized Freestream Perturbations," Doctoral Dissertation, Purdue University Aerospace Sciences Laboratory, December 1997.
25. Holden, M., "Experimental Studies of Laminar, Transitional, and Turbulent Hypersonic Flows Over Elliptic Cones at Angle of Attack," Air Force Office of Scientific Research Technical Report AFRL-SR-BL-TR-98-0142, Bolling Air Force Base, DC, 1998.
26. Schmisseur, J. D., Schneider, S. P., and Collicott, S. H., "Receptivity of the Mach 4 Boundary Layer on an Elliptic Cone to Laser-Generated Localized Freestream Perturbations," AIAA paper 1998-0532, January 1998.
27. Schmisseur, J. D., Schneider, S. P., and Collicott, S. H., "Response of the Mach 4 Boundary Layer on an Elliptic Cone to Laser-Generated Freestream Perturbations," AIAA paper 1999-0410, January 1999.
28. Lyttle, I. J., and Reed, H. L., "Use of Transition Correlations for Three-Dimensional Boundary Layers within Hypersonic Flows," AIAA-95-2293, June 1995.
29. Cheatwood, F. M. and Gnoffo, P. A., "User's Manual for the Langley Aerothermodynamic Upwind Relaxation Algorithm (LAURA)," NASA TM 4674, April 1996.
30. Candler, G., Barnhardt, M., Drayna, T., Nompelis, I., Peterson, D., and Subbareddy, P., "Unstructured Grid Approaches for Accurate Aeroheating Simulations," AIAA Paper 2007-3959, 2007.
31. http://vulcan-cfd.larc.nasa.gov/index.html
32. Chang, C.-L., "LASTRAC.3d: Transition Prediction in 3D Boundary Layers," AIAA Paper 2004-2542, 2004.
33. Mack, L.M. "Boundary Layer Stability Theory," In *"Special Course on Stability and Transition of Laminar Flow,"* AGARD R-709, pp. 3-1–3-81, 1984.
34. Nayfeh, A. H., Stability of Three-Dimensional Boundary Layers, AIAA J., Vol. 18, pp. 406-416, 1980.
35. Cebeci, T. and Stewartson, K., "On Stability and Transition of Three-Dimensional Flows," AIAA J., Vol. 18, pp. 398-405, 1980.
36. Cebeci, T. and Chen, H.H., "A Numerical Method for Predicting Transition in Three-Dimensional Flows by Spatial Amplification Theory," AIAA Paper 91-1606-CP, 1991.
37. Spall, R.E. and Malik, M.R., "Linear Stability of Three-Dimensional Boundary Layers over Axisymmteric Bodies at Incidence," AIAA J., Vol. 30, No. 4, pp. 905-913, 1992.
38. Cattafesta L.N., Iyer V., Masad J.A., King R.A. and Dagenhart J.R., "Three-Dimensional Boundary Layer Transition on a Swept Wing at Mach 3.5," AIAA Journal 33(11), November 1995.
39. Herbert, Th., "On the Stability of 3D Boundary Layers," AIAA Paper 1997-1961, 1997.
40. Hu, S. H. and Zhong, X., "Nonparallel Stability Analysis of Compressible Boundary Layer using 3D PSE," AIAA Paper 1999-0813, 1999.
41. Lin, R.-S., Malik, M. R., "On the Stability of Attachment-line boundary Layers Part 1. The Incompressible Swept Hiemenz Flow." J. Fluid Mech., Vol. 311, pp. 239-255, 1996.
42. Theofilis, V., Fedorov, A.V. and Collis, S. S., "Leading-Edge Boundary Layer Flow," Prandtl's Vision, Current Developments and Future Perspectives," International Union of Theoretical and Applied Mechanics Symposium: One Hundred Years of Boundary Layer Theory, August 2004.
43. Hall, P., Malik, M.R., and Poll, D.I.A., "On the Stability of an Infinite Swept Attachment Line Boundary Layer," Proceedings of the Royal Society of London A, vol. 395, p. 229, 1984.
44. Berger, K., Rufer, S, Kimmel, R., and Adamczak, D. "Aerothermodynamic Characteristics of Boundary Layer Transition and Trip Effectiveness of the HIFiRE Flight 5 Vehicle," Submitted to 39th AIAA Fluid Dynamics Conference, San Antonio, TX, June 2009.
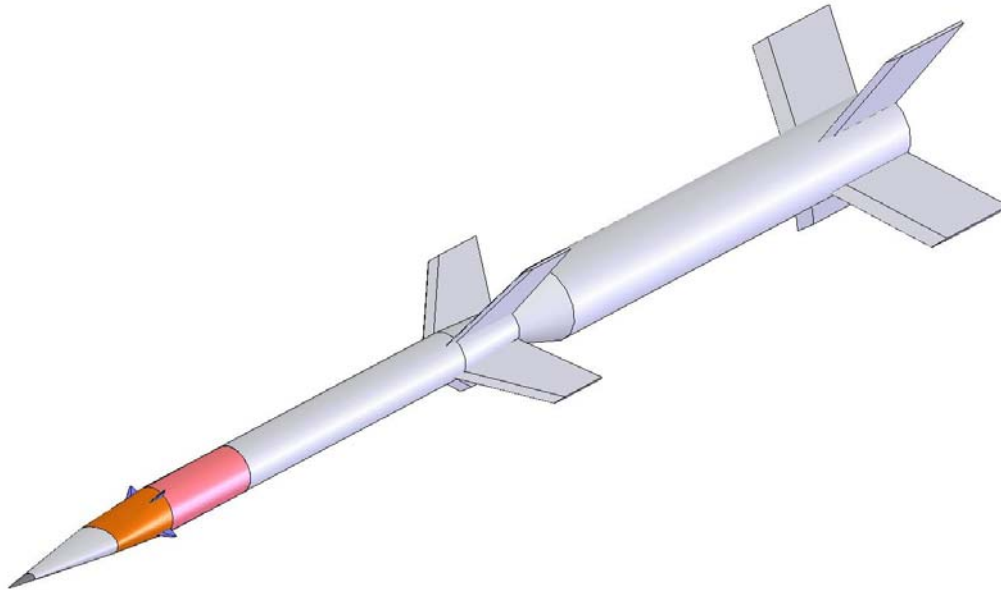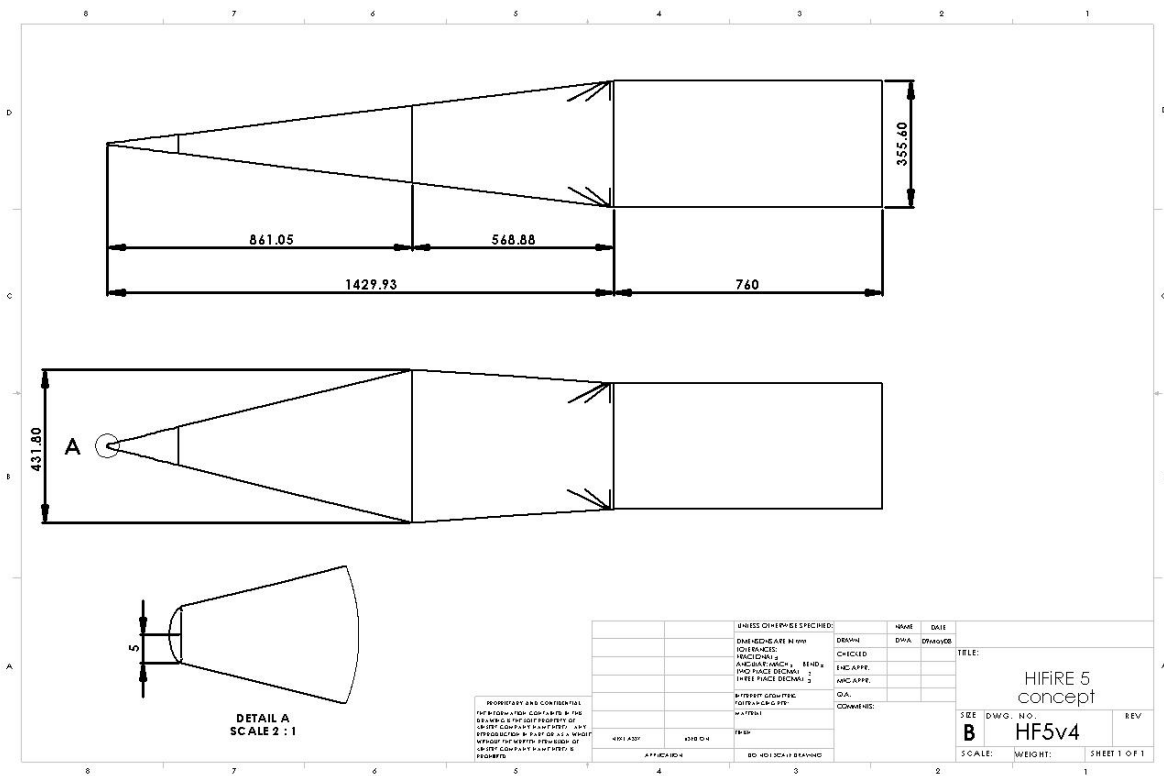
Figure 2.1 HIFiRE-5 configuration

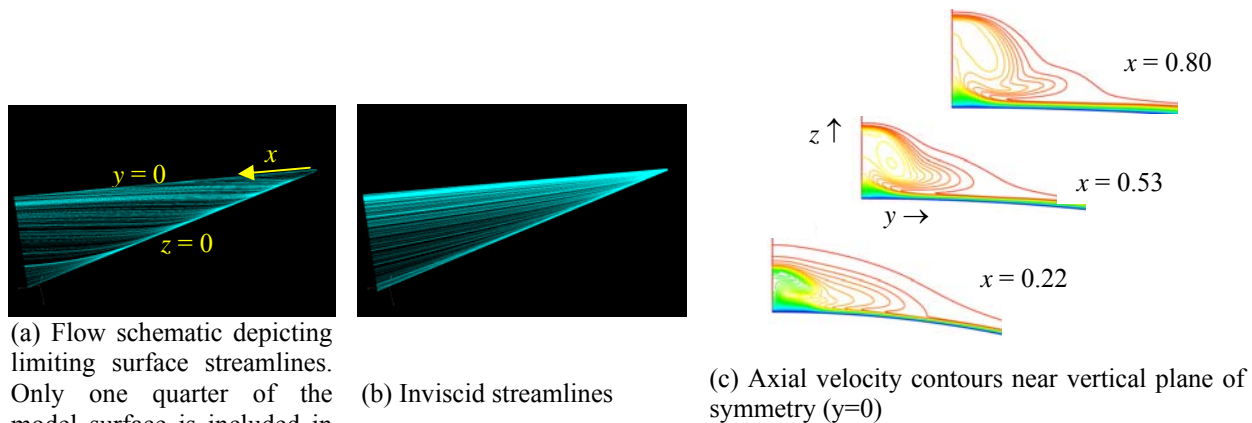**Figure 2.2 HIFiRE-5 test article concept. Dimensions in mm.**

American Institute of Aeronautics and Astronautics

(a) Flow schematic depicting limiting surface streamlines. Only one quarter of the model surface is included in the figure

(b) Inviscid streamlines

(c) Axial velocity contours near vertical plane of symmetry (y=0)

Figure 4.1. Mean flow for the HIFiRE-5 forecone at h = 18 km trajectory point (y=0 and z=0 correspond to minor and major axis planes of symmetry, respectively)

(a) Re_θ/M_e

(b) Crossflow Reynolds number R_{cf}

(c) Attachment line Reynolds number with compressibility correction as defined in ref. [1]. Corresponding values for three other test conditions including the h = 33 km flight conditions are also shown. For the wind tunnel cases, the abscissa is scaled to the full scale model.
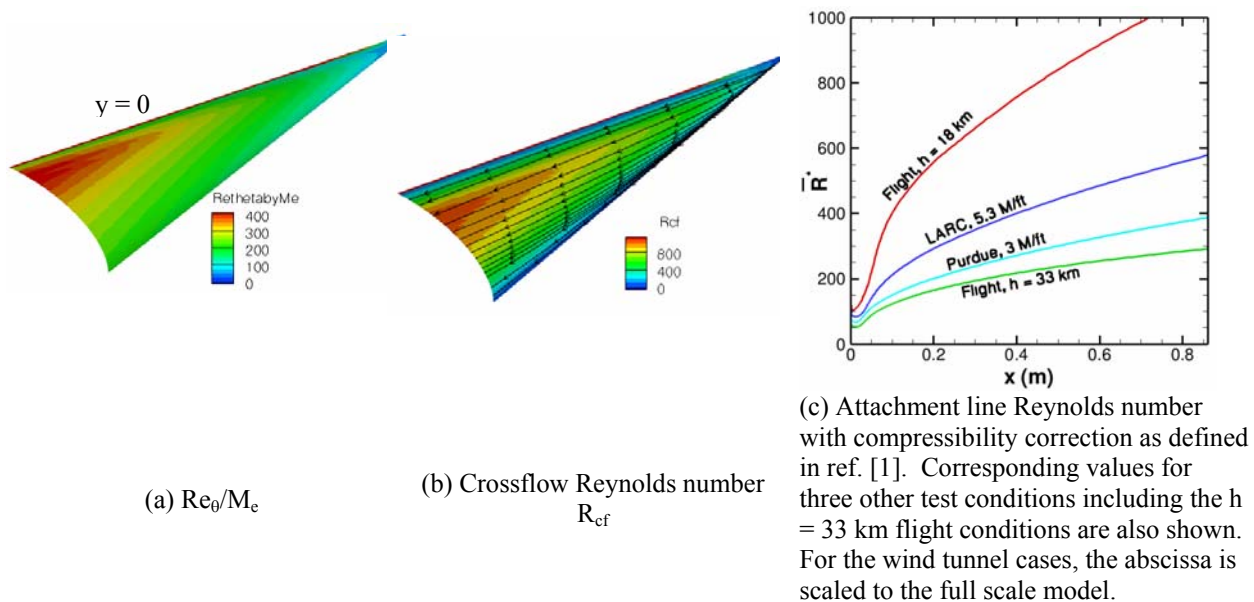
Figure 4.2. Mean flow parameters relevant to boundary layer transition

(a) Second mode instability (Note: There is a very thin region of high N factors near the upper boundary.)

(b) Stationary crossflow modes

(c) Traveling crossflow modes
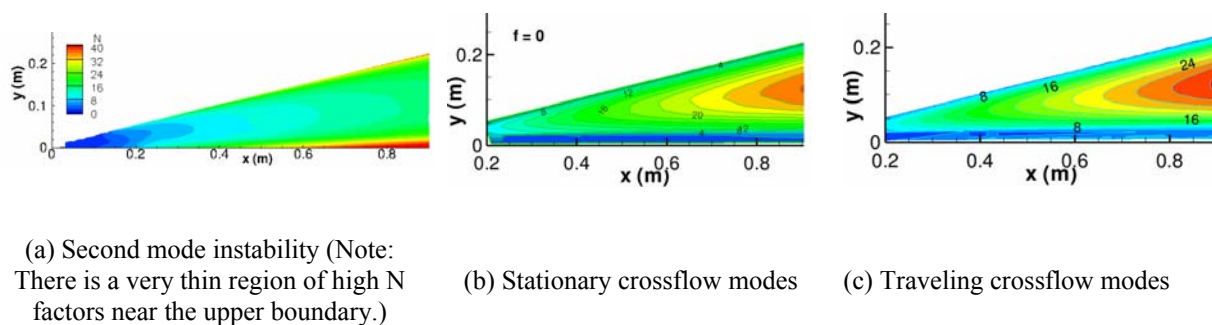
Figure 4.3. Contours of logarithmic amplification ratio (N factor) for relevant types of instabilities
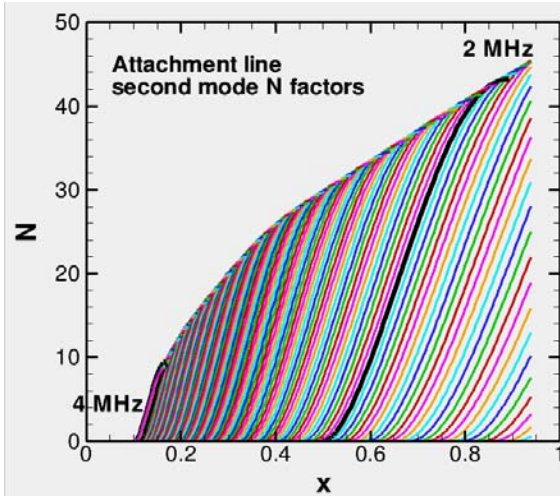
(a) N-factor evolution along attachment line (abscissa in meters)
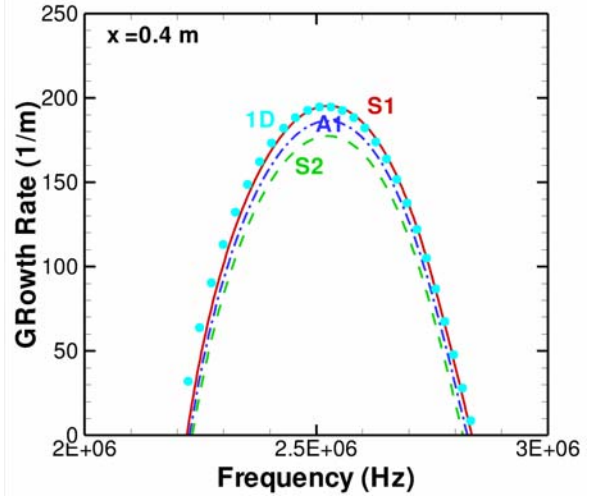
(b) Growth rate vs. disturbance frequency at x = 0.4 m, showing both 1D (i.e., ODE based) and 2D (i.e., PDE based) eigenvalue solutions

Figure 4.4. Instability characteristics along attachment line
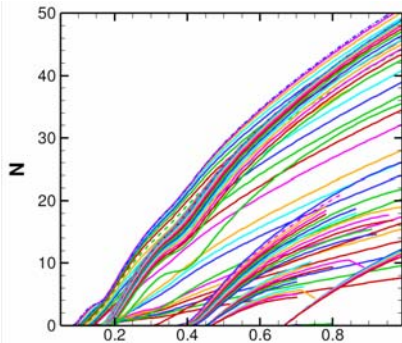
(a) N-factor evolution for 2D disturbances of various frequencies
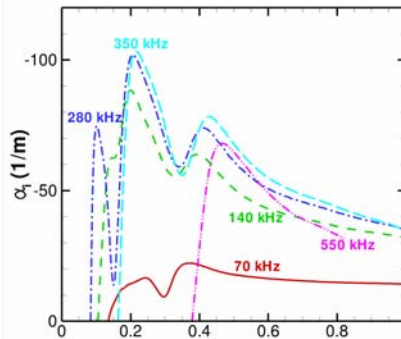
(b) Streamwise distribution of amplification rates for disturbance modes at selected frequencies
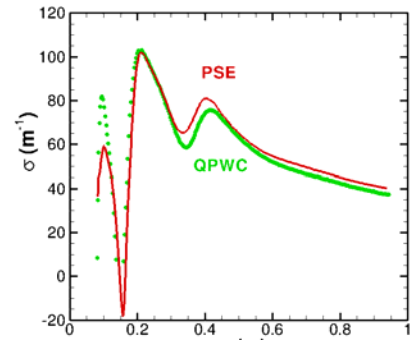
(c) Spatial growth rate of 2D disturbance at f = 300 kHz along the y=0 symmetry line. Peak difference in respective N-factors is less than 2, whereas the maximum N factor at x = 0.861 m is 46.5

Figure 4.5. Instability characteristics along minor axis plane of symmetry (y=0). Abscissa in all figures corresponds to axial coordinate x in meters.

(a) |T| mode shapes

(b) |u| mode shapes

(c) Real part of temperature fluctuation, T_r
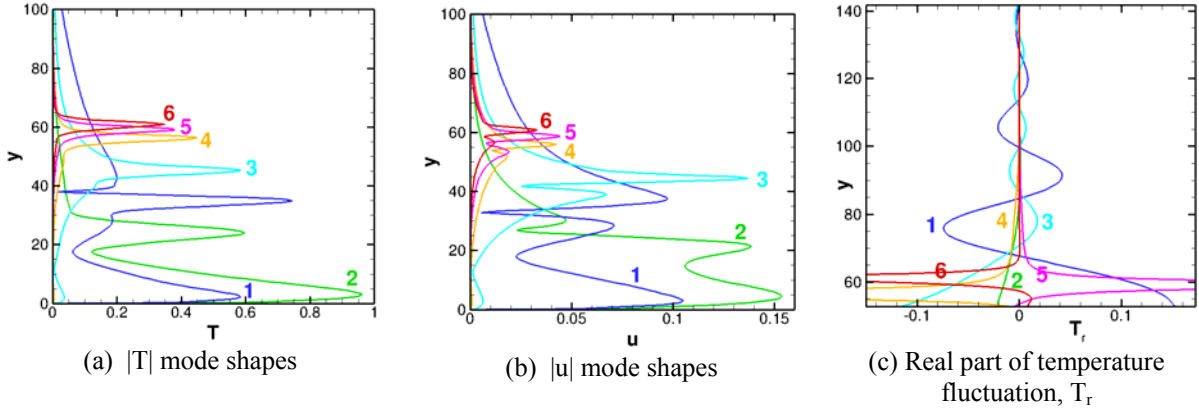
Figure 4.6. PSE mode shapes for 2D disturbance at f = 300 kHz at selected locations along the minor axis plane of symmetry. Locations 1 to 5 correspond to the three peaks and two valleys of the growth rate variation depicted in Fig. 4.5c, whereas location 6 corresponds to a representative location aft of the third and last peak in growth rate distribution. Ordinate is scaled with respect to local boundary layer length scale.
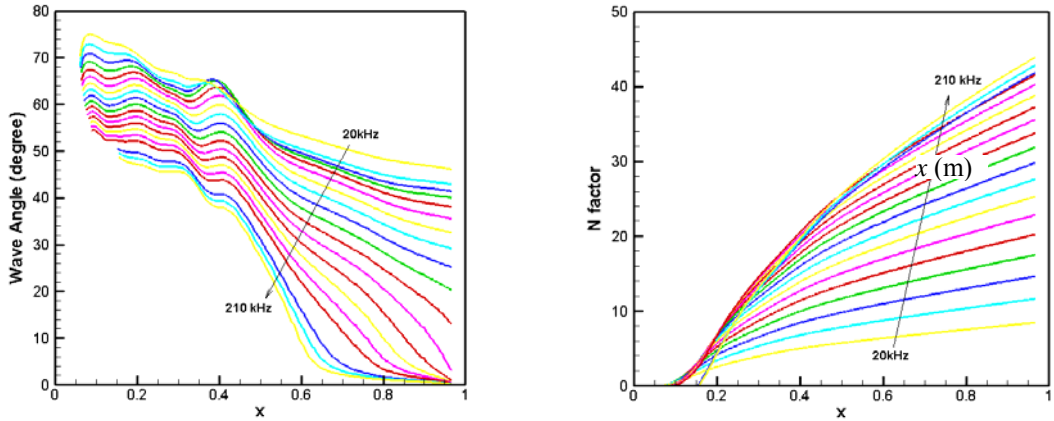
(a) Wave angle of 3D disturbances with highest local growth rate as a function of frequency parameter (wave angle is measured with respect to local flow direction)

(b) N-factor curves for fixed frequency disturbances based on local growth rate maximization over β (envelope method)

Figure 4.7. 3D instability modes along y=0 meridian
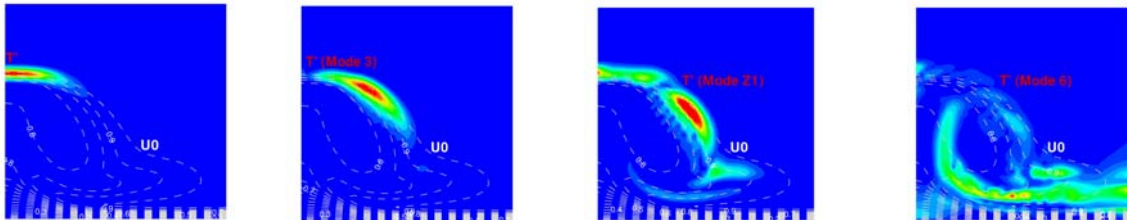
Figure 4.8. Mode shapes predicted by partial-differential-equation-based, planar eigenvalue analysis near the vertical plane of symmetry at x = 0.7m. (Dashed white contours indicate the distribution of mean axial velocity; bottom boundary corresponds to solid wall, left boundary corresponds to minor axis plane y=0; vertical extent of each plot is equal to 0.0147m.)
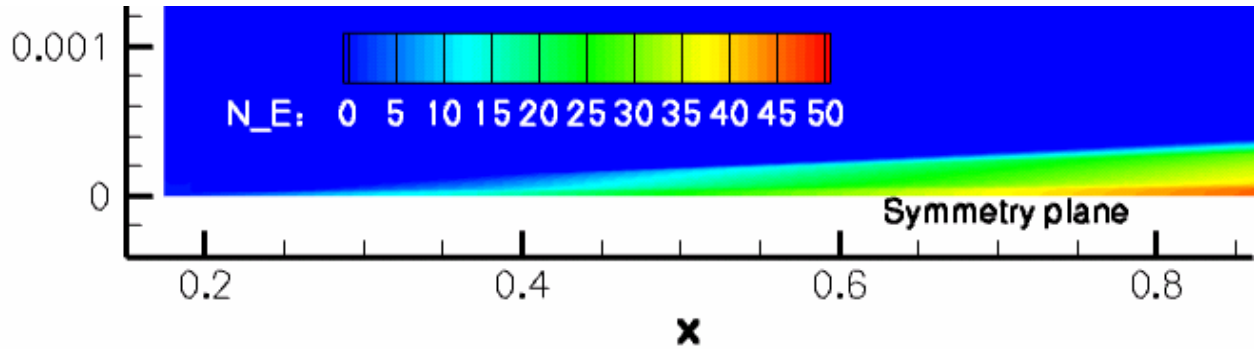
Figure 4.9. N-factor distribution for disturbance mode with f = 400 kHz as predicted via surface marching PSE analysis. Amplitude is plotted on a logarithmic scale, relative to the initial amplitude at the boundary of the computational domain. Both abscissa and ordinate are in meters.

(a) Based on mode tracking for constant axisymmetric mode number, m_β

(b) Based on local growth rate maximization over β (envelope method)
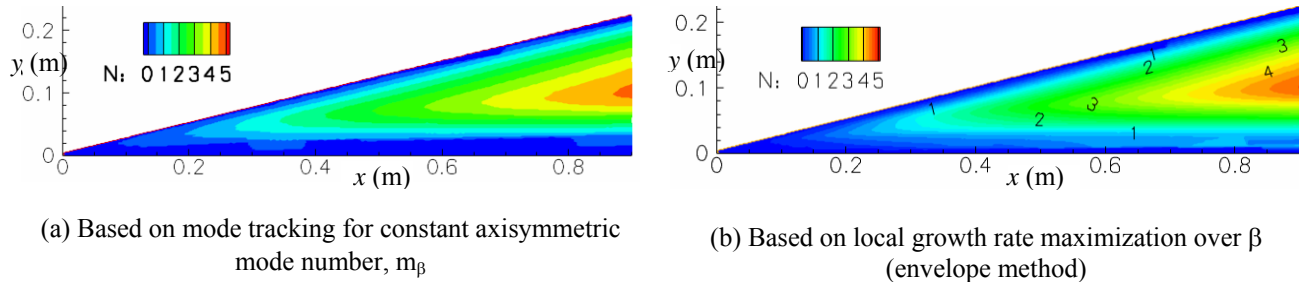
Figure 4.10. N-factor distribution for stationary crossflow vortices (flight conditions at h = 33 km)

Off-Surface Flow:
u velocity contours

Surface Heating Distribution
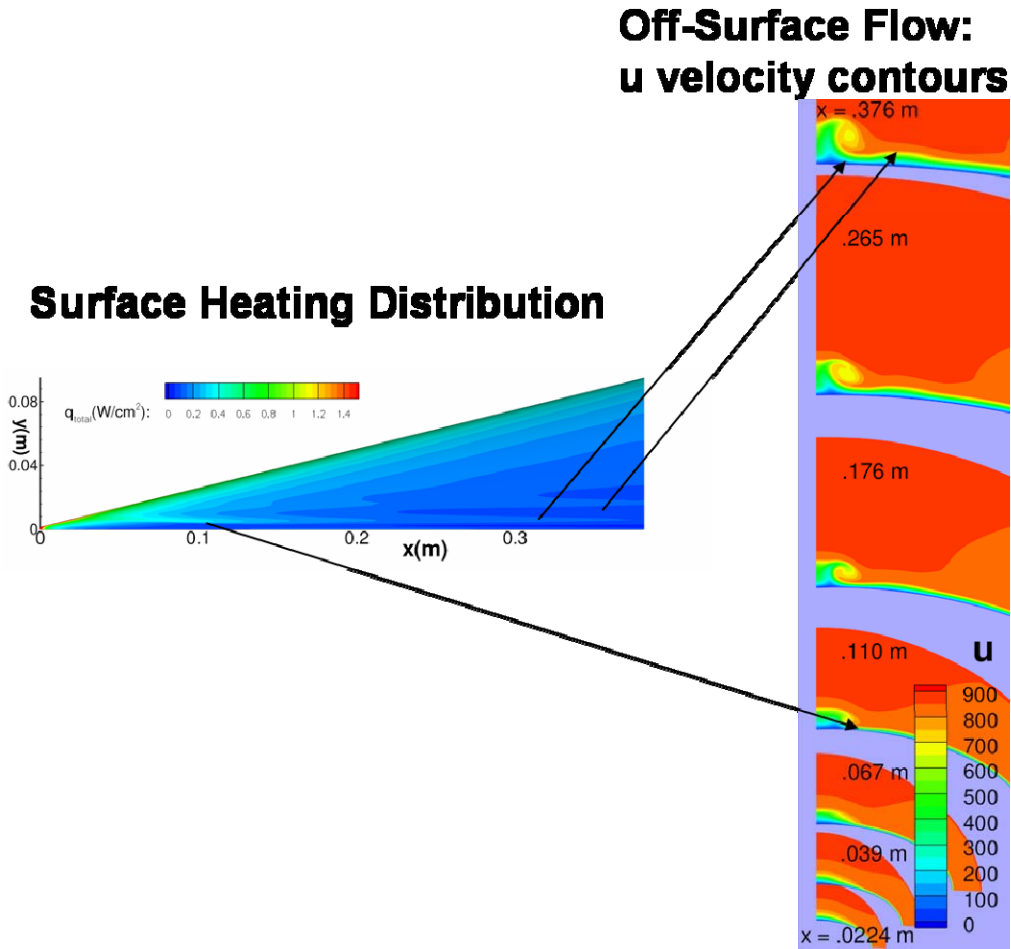
Figure 5.1. Mean flow characteristics for the Purdue wind tunnel configuration at Re=3M/ft
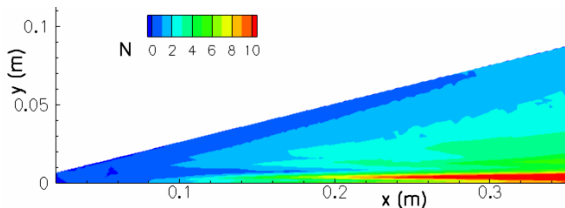
Fig. 5.2(a) N-factor distribution based on quasi-parallel linear stability theory. (The jaggedness in contours is caused by coarseness of grid along the surface and/or along the frequency axis.)
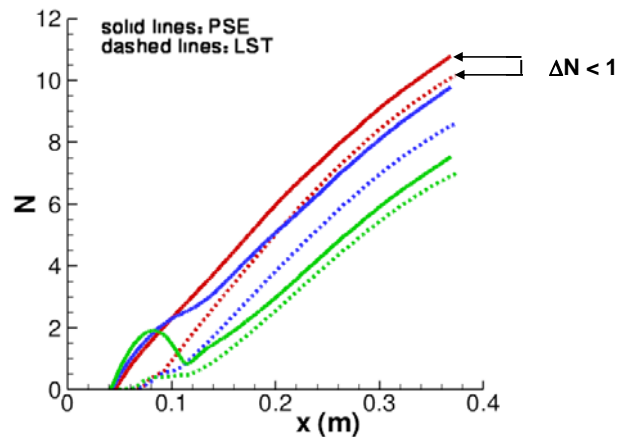
Fig. 5.2(b) Effect of mean-flow non-parallelism on N-factor curves for disturbances in the range of most amplified frequencies along y=0 symmetry plane (f ≈90–100 kHz): Comparison between linear stability theory (LST) and PSE

Figure 5.2. Logarithmic amplification ratio (N factor) for 2D streamwise instabilities
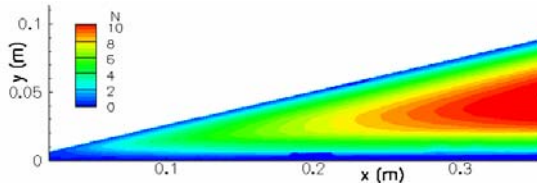
(a) Based on local growth rate maximization over β (envelope method) , with integration along streamline trajectorv
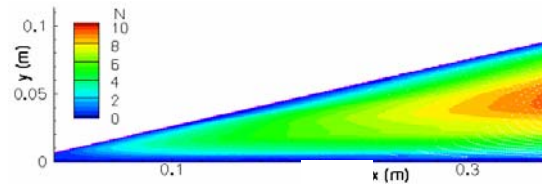
(b) Based on mode tracking for constant β

(c) Based on local growth rate maximization over β (envelope method), with integration along group velocity trajectory

(d) Based on mode tracking for constant axisymmetric mode number, m_β

Figure 5.3. N-factor distribution for stationary crossflow vortices
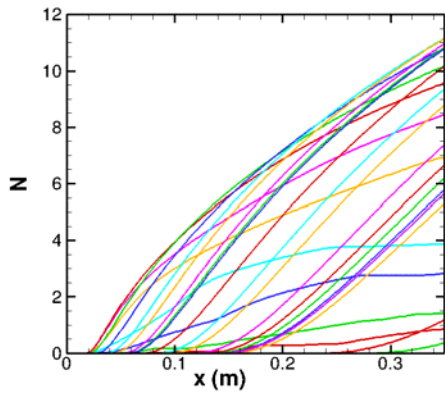
(a) Based on local growth rate maximization over β (envelope method) , with integration along streamline trajectory
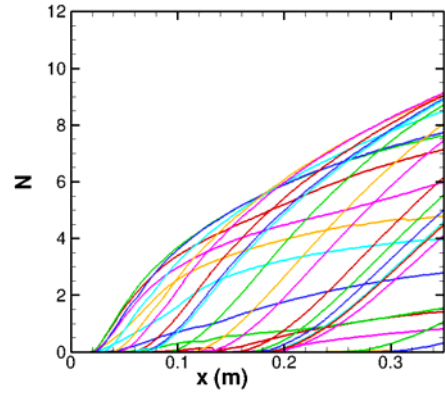
(b) Based on mode tracking for constant β
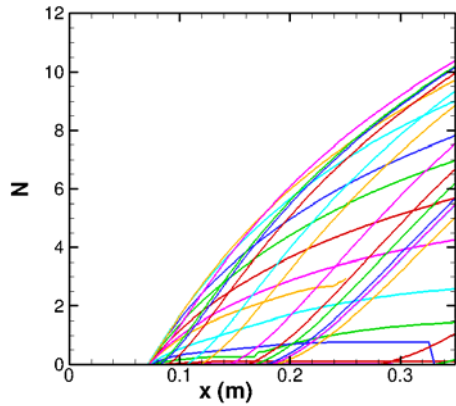
(c) Based on local growth rate maximization over β (envelope method), with integration along group velocity trajectory
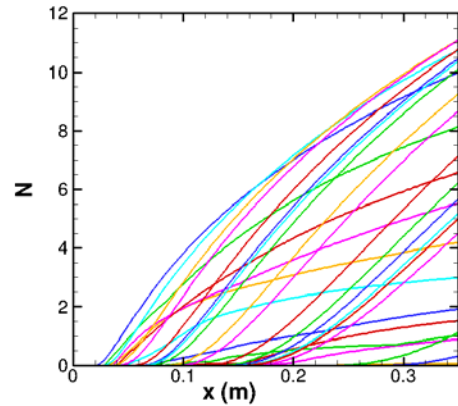
(d) Based on mode tracking for constant axisymmetric mode number, m_β (where m_β denotes the number of waves across the circumference)

Figure 5.4. N-factor evolution along selected surface trajectories for stationary crossflow vortices
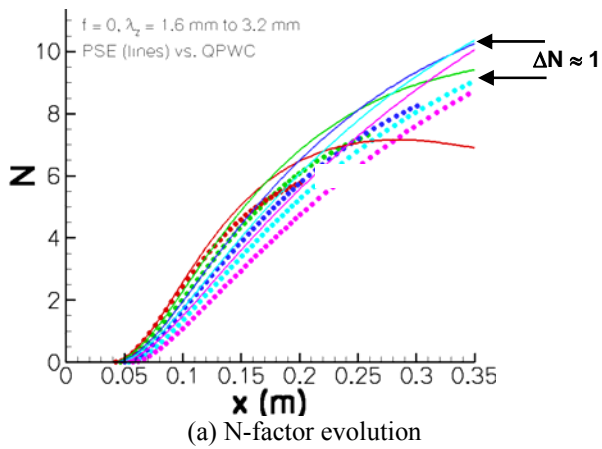
(a) N-factor evolution
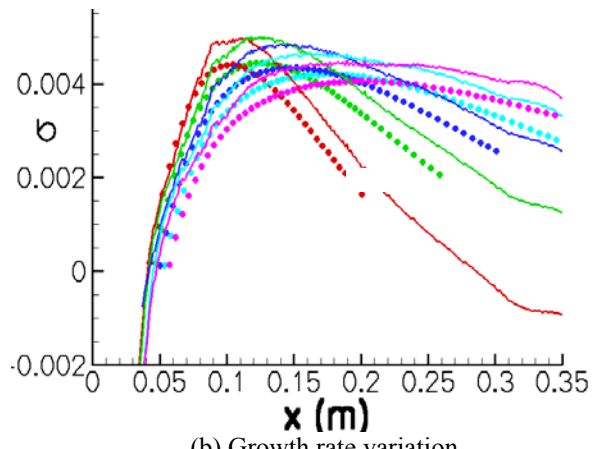
(b) Growth rate variation

Figure 5.5. Amplification characteristics of stationary crossflow vortices along a selected trajectory within the region of peak stationary crossflow N factors. Lines denote PSE predictions, whereas symbols indicate quasi-parallel theory with curvature effects included (QPWC).
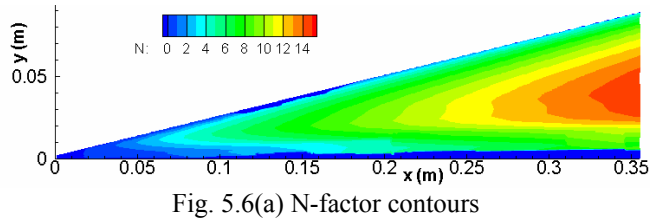
Fig. 5.6(a) N-factor contours
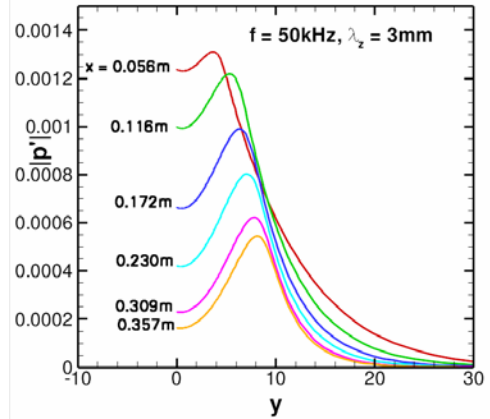
Fig. 5.6(b) p' eigenfunctions at selected x locations along a particular integration trajectory within the region of dominant crossflow growth

Figure 5.6. Traveling mode instabilities
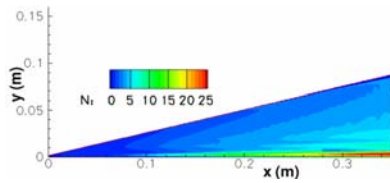
(a) 2D streamwise instability
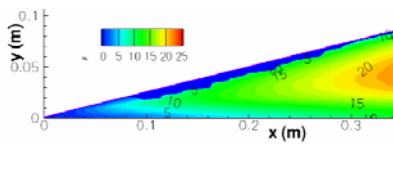
(b) Traveling crossflow modes

Figure 5.7. Contours of logarithmic amplification ratio (N factor) for different instability modes for the LARC Mach 6, α=0, β=0 configuration with Re=5.3M/ft
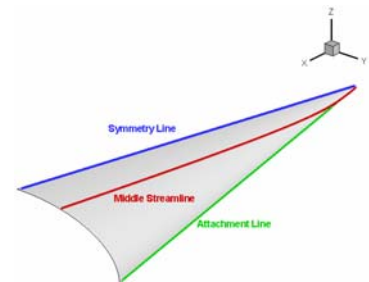
Figure 5.8(a). Three N-factor integration paths used to assess non-parallel effects.
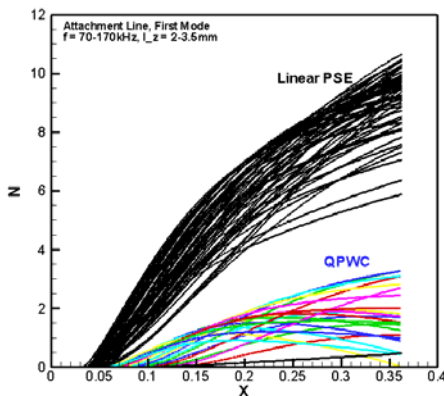

Fig. 5.8(b)
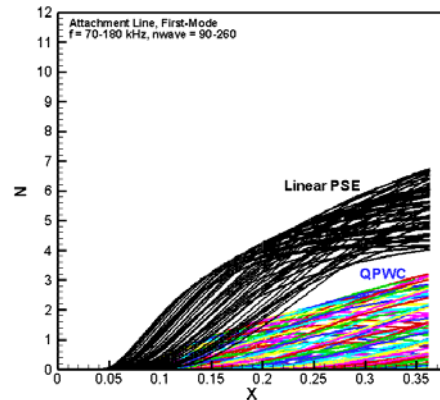
Fig. 5.8(c)

Figure 5.8 Comparison of QPWC and linear PSE N-factor calculated by tracking a broad set of individual modes with a specified frequency and (b) fixed spanwise wavelength (c) fixed integer azimuthal wave number m_β, both along the attachment line path. (Each curve corresponds to a specific combination of frequency and wavelength/azimuthal wave number; the overall envelope of these curves determines estimated transition behavior.)
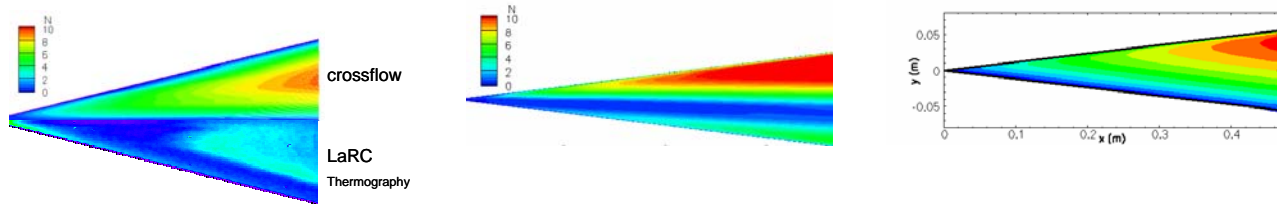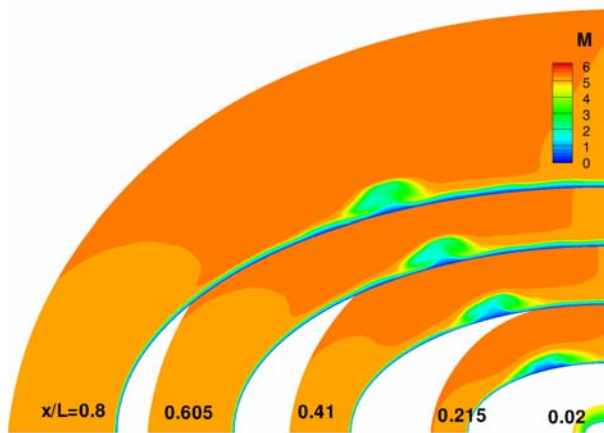
(a) HIFiRE-5: α = 0° (plan view) Bottom half corresponds to data from Langley experiments [44] at approximately same Reynolds number.

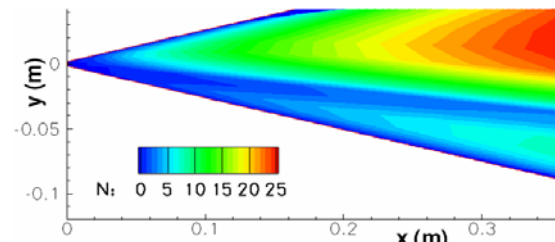(b) HIFiRE-5: α = 4° (side view)

(c) Purdue 7-deg circular cone: α = 6° (side view) — results based on ref. [10].

Figure 5.9. Effect of angle of attack and model cross-section on N-factor contours for HIFiRE-5 and Purdue 7-deg cone models

(a) Mach number contours at selected x locations

(b) N-factor contours for stationary ctossflow modes

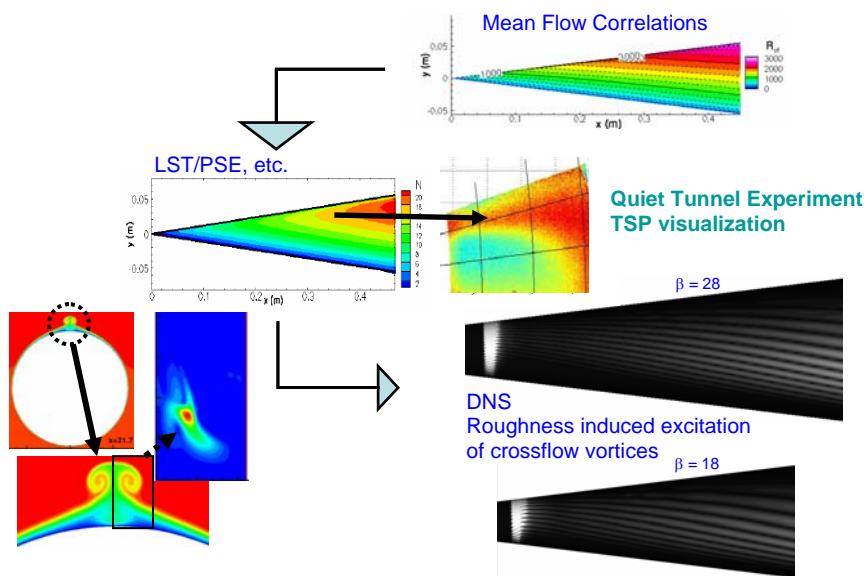Figure 5.10. N-factor distribution for stationary crossflow vortices (LARC M=6, Re=5.6M/ft, β=4 deg)

Figure 6.1. Application of variable fidelity analysis tools in the context of 7-deg circular cone at 6-deg AOA. The quiet tunnel image was provided by Dr. E. Swanson and Prof. Schneider of Purdue University [9].

American Institute of Aeronautics and Astronautics